Anharmonic quantum effects of implanted muons: Route to probing nuclear quantum behavior in solids

F. Hotz [1,*] M. Gomilšek [2,3,†] T. Arh [1] T. J. Hicken [1] P. Umek [2] A. Zorko [2,3] and H. Luetkens [1]

[1] *PSI Center for Neutron and Muon Sciences CNM, CH-5232 Villigen PSI, Switzerland*

[2] *Jožef Stefan Institute, Jamova cesta 39, SI-1000 Ljubljana, Slovenia*

[3] *Faculty of Mathematics and Physics, University of Ljubljana, Jadranska ulica 19, SI-1000 Ljubljana, Slovenia*

(Received 17 July 2025; revised 18 March 2026; accepted 7 April 2026; published 8 June 2026)

The quantum behavior of light particles in solids gives rise to phenomena that cannot be captured by a classical description. We show that muon spin spectroscopy (μSR), when paired with a quantum-mechanical treatment of the implanted muon, becomes a sensitive and direct probe of nuclear quantum effects. By modeling the muon as a spatially extended quantum particle, our approach captures strong anharmonic behavior. We demonstrate this in Zn-barlowite, which serves as a nontrivial test case due to its structurally complex lattice and the presence of both fluorine and hydroxyl groups. Our results establish a route for extracting nuclear quantum signatures from μSR data and open different opportunities for studying light nuclei such as hydrogen and lithium in systems where quantum fluctuations shape structure and function.

DOI: 10.1103/x1y3-9chs

Materials containing light nuclei, such as hydrogen or lithium, play a key role in many important material classes, including superconductors, hydrogen-storage materials, semiconductors, Li-ion batteries, and other advanced technologies [1–5]. To understand these materials careful consideration of quantum-mechanical effects is required, such as uncertainty in nuclear positions, a finite zero-point energy, and quantum tunneling, which can profoundly influence their properties. Accurately capturing these phenomena requires advanced computational methods that can address their complex interplay [1,6,7]. Therefore, there is a pressing need for approaches that seamlessly integrate nuclear quantum effects into *ab initio* descriptions of matter, paving the way for a deeper understanding of many, inherently quantum, materials. However, the development of accurate and efficient *ab initio* methods is hindered by the difficulty of experimentally determining the precise impact of these quantum effects.

Muon spin spectroscopy (μSR) offers a unique insight by being able to directly measure the quantum behavior of light particles in solid-state environments [8–10]. In μSR, positive muons—charged (anti)particles $\sim 9\times$ lighter than protons—are implanted into a material, where they interact with the surrounding magnetic and electronic fields. Their low mass enhances their sensitivity to quantum effects, by increasing their wave-function spread (i.e., their quantum uncertainty in position), boosting zero-point energy (ZPE), and speeding up quantum tunneling. μSR enables direct measurement of these effects through dipolar interactions between the magnetic moment of the muon and those of the surrounding nuclei and electrons [11–14]. Muons thus act as ideal proxies for studying the general quantum behavior of light particles in materials. This can most clearly be seen in cases where classical, point-particle descriptions of muons fail to adequately describe experimental μSR data, promoting the need for a quantum description of muons [15–17]. By combining advanced *ab initio* [density functional theory (DFT)] and muon wave-function calculations with μSR experiments, a much deeper understanding of light particles in matter can be achieved. We demonstrate this for the case of Zn-barlowite [18–21], where we find that the average muon positions are shifted from those based on classical predictions by strong quantum anharmonic effects, while the stability of different candidate muon stopping sites are significantly impacted by quantum ZPE. We confirm these *ab initio* predictions by precision μSR experiments. We selected Zn-barlowite for this study because, as a candidate quantum spin liquid (QSL), it is a material of broad current interest [22–27]. Zn-barlowite offers a nontrivial environment in which to test the quantum behavior of the implanted muon. Its lattice [Fig. 1(a)], which includes both fluorine and hydroxyl groups, provides an ideal environment for observing pronounced anharmonic effects, owing to the strong coupling between the muon spin and the spins of surrounding electronegative ions—enabling a direct measurement of the muon's quantum response. Using DFT to simulate classical muons in a DFT + μ approach [12] (see the Appendix A for details) we predict four distinct classical muon stopping sites. The muon forms a μ-OH complex at three of them [Figs. 1(b)–1(d)] that are very close in energy (Table I), while at the fourth site, the muon forms a F-μ-Br complex [Fig. 1(e)] with a classical energy 0.6 eV higher than at the lowest μ-OH site. A large occupancy of this higher-energy site was found in a prior experiment [21], however, this seems to be in conflict with the heuristic expectation that

*Contact author: fabian.hotz@psi.ch

†Contact author: matjaz.gomilsek@ijs.si

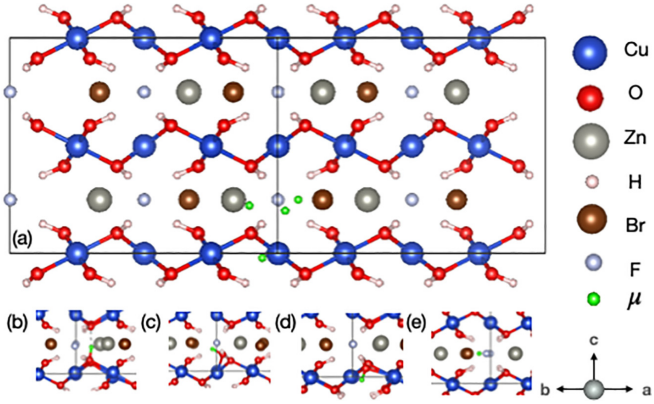

FIG. 1. (a) Candidate muon stopping sites in Zn-barlowite identified using classical DFT + μ (green) in the undistorted $2 \times 2 \times 1$ supercell. (b)–(d) Close-up views of the μ-OH sites, showing local distortions induced by the muon. (e) F-μ-Br stopping site with its associated local distortion.

only sites with energies within approximately 0.5 eV of the lowest-energy site are typically occupied [8,12,28].

The first and most accessible approximation to improve the classical point-particle description of DFT + μ is the quantum harmonic approximation, valid for small displacements of the muon from its classical position [15]. Neglecting the quantum entanglement of muon and nuclear positions, the muon ZPE for each site can be estimated by summing the contributions $\hbar\omega_j/2$ of the three main Γ-point normal phonon modes ω_j calculated by DFT with the muon embedded in the crystal [15,29]. This leads to total muon site energies listed in Table I.

The relative stability of the highest-energy F-μ-Br site is improved from the classical calculations by taking into account the quantum ZPE. However, since at this site the muon is shared between strongly electronegative F^{-1} and Br^{-1} ions, the potential could be strongly anharmonic, making the harmonic approximation insufficient. Furthermore, as the highest-frequency normal mode at the μ-OH sites is along the μ-O direction, one could expect strong anharmonic effects also at μ-OH sites, with a higher-energy penalty for displacements towards the oxygen than away from it due to the positive muons being electrostatically repulsed from the positive nucleus of oxygen.

To distinguish between the harmonic and anharmonic scenarios, we turn to experiment. The aim is to determine the unique nuclear neighborhoods and muon wavefunctions at sites F-μ-Br and μ-OH in Zn-barlowite, exploiting the coupling between muon and nuclear spins [8,30,31]. For this purpose, longitudinal-field (LF) μSR experiments were performed on Zn-barlowite powder samples on the FLexible Advanced MuSR Environment (FLAME) instrument at PSI, Switzerland, in fields up to 4 mT (Fig. 2).

TABLE I. A comparison of classical and quantum (classical+ZPE) muon energies in the harmonic and anharmonic effective potentials for the four candidate muon stopping sites, relative to the lowest-energy site (μ-OH)$_1$. Δr_μ is the absolute quantum anharmonic shift of the average muon position from the classical position.

	(μ-OH)$_1$	(μ-OH)$_2$	(μ-OH)$_3$	F-μ-Br
Classical (eV)	0	0.0	0.1	0.6
Harmonic (eV)	0.9	0.9	1	1.3
Anharmonic (eV)	0.9	1	1.1	1.2
Δr_μ (Å)	0.17	0.12	0.08	0.06

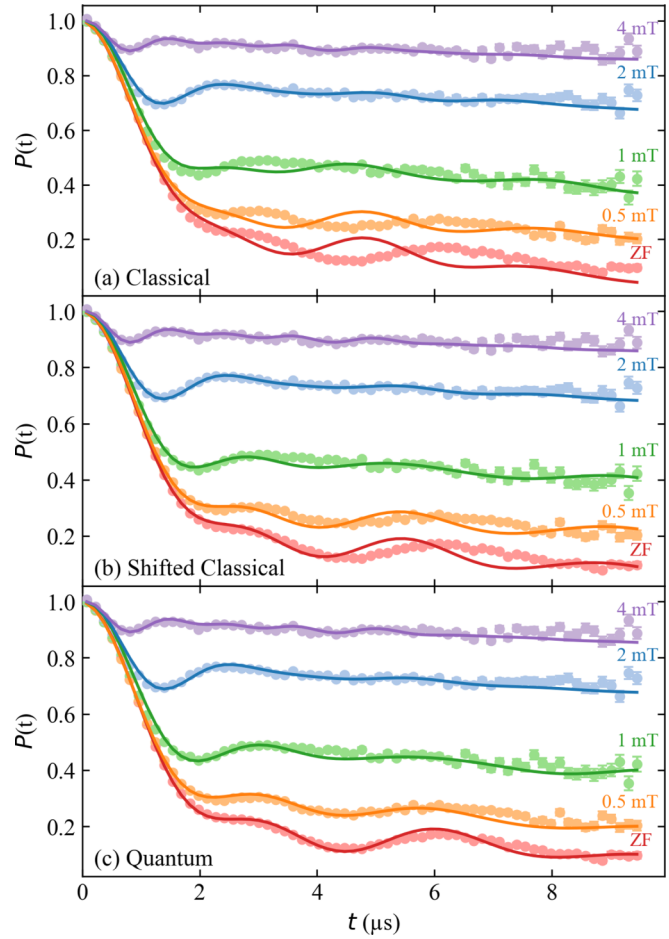

FIG. 2. Experimental LF decoupling μSR data on Zn-barlowite (points) at 20 K, fitted using Eq. (1) (curves) assuming (a) a classical muon position, (b) a point-particle muon shifted to the average quantum muon position (Fig. 3), and (c) a fully quantum muon.

To check whether the predicted muon stopping sites account well for experimental data we compute the time evolution of the muon polarization due to dipolar interactions with nuclear spins at each of the four muon sites i via exact-diagonalization calculations, giving $P_i^{\text{stat}}(t) = \langle \frac{1}{2}\text{Tr}\{\sigma_{\hat{n}}^{\mu} \exp(\frac{i}{\hbar}\hat{\mathcal{H}}_i t)\sigma_{\hat{n}}^{\mu} \exp(\frac{-i}{\hbar}\hat{\mathcal{H}}_i t)\}\rangle_{\hat{n}}$, where $\sigma_{\hat{n}}^{\mu}$, is the muon's Pauli spin operator in the detector direction $\hat{n}$ relative to a powder grain, and $\langle\cdots\rangle_{\hat{n}}$ represents a powder average [8,31–33]. The Hamiltonian $\hat{\mathcal{H}}_i$ consists of the Zeeman interaction due to the external applied field B, dipolar interactions between the muon and nuclear spins, and quadrupole interaction of the Br nuclei (spin $I = 3/2$) with the local electric field gradient [15,34]. The latter two terms depend on the muon position, providing experimental sensitivity to the muon position. Furthermore, the electron spins of magnetic Cu^{2+} ions remain disordered and fluctuate in the QSL ground state

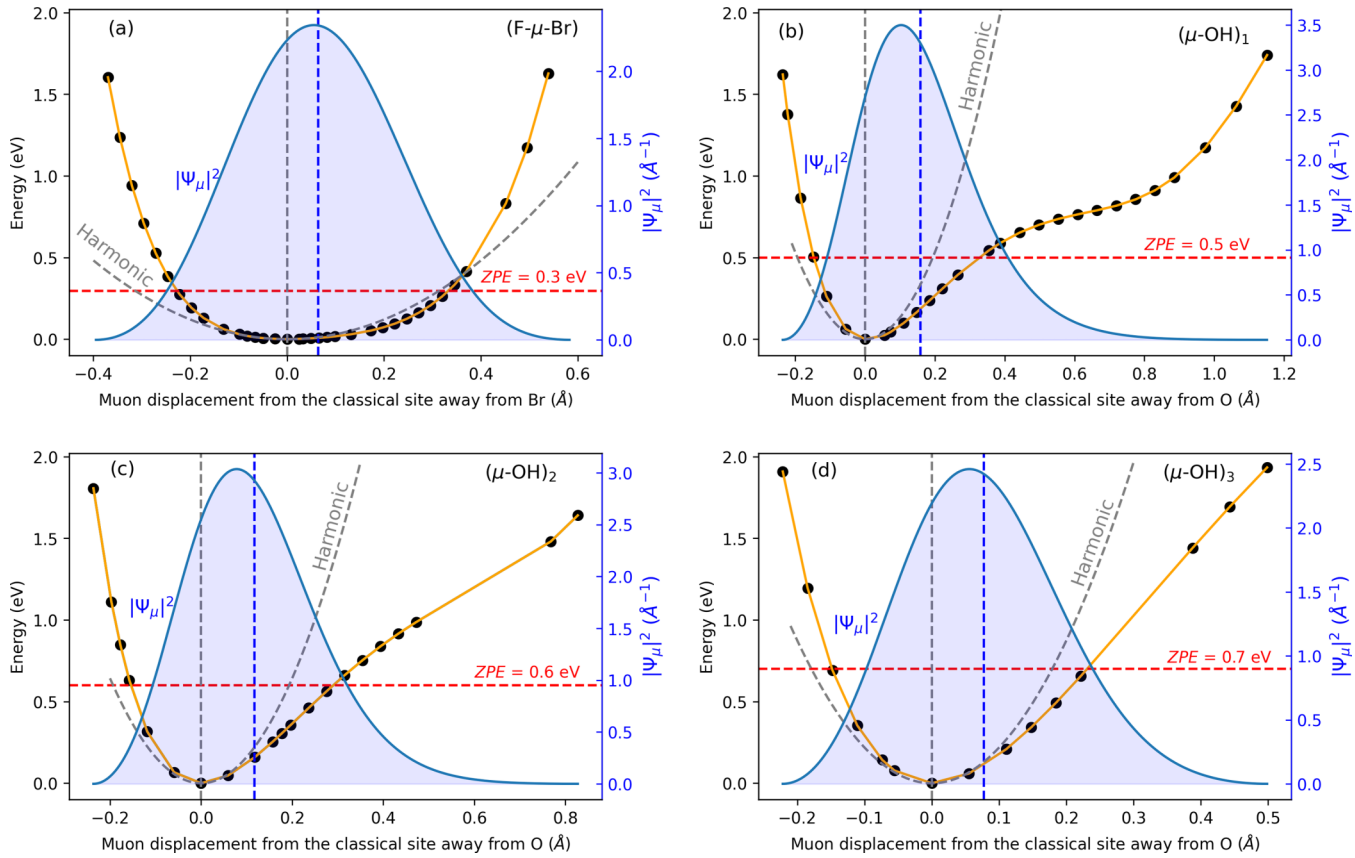

FIG. 3. Effective potentials in the weakly bound adiabatic limit (relative to the classical energy) for muon displacements along the (a) F-Br and (b)–(d) $(\mu\text{-O})_i$ directions at F-μ-Br and μ-OH sites, respectively, from DFT (black points, interpolated by orange curves). These are compared to the effective potential under the harmonic approximation (dashed gray). Also shown here, the quantum muon probability distributions $|\psi_\mu|^2$ in the adiabatic potentials (blue curves) with the resulting average muon displacements Δr_μ (dashed vertical blue lines) away from their classical/harmonic positions (dashed vertical gray lines).

of Zn-barlowite [18,20,21,35], further dynamically relaxing the muon's spin. Due to these fluctuations, the final muon polarization at a given muon site can be written as [8,10] $P_i(t) = P_i^{\text{stat}}(t)P^{\text{dyn}}(t)$. Here, the contribution due to electron spin fluctuations is accounted for by the exponential function $P^{\text{dyn}}(t) = \exp(-\lambda_{\text{dyn}}t)$, where λ_{dyn} is the dynamical relaxation rate, which depends on the applied field B. Although each local surrounding could have a different relaxation rate λ_{dyn} the final fits are not noticeably improved by allowing this, so we constrain λ_{dyn} to be equal at all sites to minimize the number of free parameters.

Adding the contributions from all muon sites together, we obtain the final fitting function for the muon polarization

$$P(t) = f_s \sum_{i=0}^{4} f_i P_i(t) + (1 - f_s)P_{\text{bgd}}(t), \tag{1}$$

where f_s is the fraction of muons that stop in the sample and f_i is the fraction of those muons that end up at a site i with polarization $P_i(t)$ (see above), where $i = 0$ denotes the F-μ-Br site and $i = 1, 2, 3$ to the three $(\mu\text{-OH})_i$ sites, respectively. $P_{\text{bgd}}(t)$ is the LF Gaussian Kubo-Toyabe function under an applied field [36], which describes the background contribution of muons that stop outside of the sample. Most importantly, the muon stopping position $\mathbf{r}_\mu$ entering the polarization functions $P_i(t)$ is fixed directly from a given classical or quantum muon site calculation, as described above, and is not allowed to vary as a fitting parameter. The fitting procedure is thus limited to determining the relative muon fractions f_i, the sample fraction f_s, and the dynamical relaxation rates. The spectra from all five applied fields are fitted simultaneously with this global set of fitting parameters.

Fit results using Eq. (1) for a muon treated as a classical point particle at the classical DFT + μ position are shown in Fig. 2(a) and summarized in Table III in Appendix C. These yield a reduced χ^2/degree of freedom (DOF) = 9.8, showing that the classical prediction fails to reproduce the experiment. The discrepancy is especially prominent at low applied fields. To improve the fit accuracy we need to model the muon wave function. To incorporate anharmonic muon effects, we have calculated the effective (adiabatic) anharmonic potential for the muon around each candidate stopping site under the assumption of negligible muon-nuclear entanglement in position (giving a single-particle, weakly bound adiabatic potential [15]), and assuming a separable potential for the muon with eigenaxes oriented along the normal mode directions obtained from the harmonic phonon DFT calculation. The effective potentials along the most anharmonic directions at the four muon stopping sites are shown in Fig. 3, while the potential along the perpendicular directions at these sites are found

to be nearly harmonic (see Appendix B). Along each normal direction, the resulting one-dimensional (1D) Schrödinger equation for the muon wave function was solved numerically using a finite-difference method. At the F-μ-Br site, the potential along the F-Br direction is flatter than expected from the harmonic approximation [Fig. 3(a)], reducing the muon ZPE and stabilizing this site (see Table I). Since the muon is located between two negatively charged ions, the average muon position is shifted by $\Delta r_\mu \approx 0.06$ Å away from the Br^- compared to the classical site. On the other hand, at μ-OH sites the adiabatic potentials along the μ-O directions are highly anharmonic, shifting the average muon position by up to 0.17 Å [Figs. 3(b)–3(d) and Table I], which represents a significant fraction of the expected 1-Å μ-O distance for a classical muon.

The fits to the μSR spectra can already be improved by shifting a point-particle muon, from the classical to the average quantum position, which is anharmonically shifted away from the classical one by Δr_μ (Table I), as shown in Fig. 2(b). This yields $\chi^2/\mathrm{DOF} = 3.5$. However, the fit quality is further substantially improved by taking into account the quantum uncertainty in muon position; in other words, using its full computed wave function ψ_μ to construct an effective muon-nuclear spin hamiltonian, by averaging point-particle dipolar muon-nuclear hamiltonians over the muon probability distribution $|\psi_\mu|^2$ [15]. The result is shown in Fig. 2(c), which yields the final reduced $\chi^2/\mathrm{DOF} = 1.9$. This good agreement between experimental data and calculation validates our fully quantum approach to an *ab initio* treatment of implanted muons. Our results show that to determine the muon stopping sites in compounds with strongly electronegative ions such as F^-, Cl^-, and Br^-, or functional groups, such as OH^-, it is necessary to treat the muon as a quantum particle in an anharmonic potential. Additionally, this approach provides a way towards understanding the quantum anharmonic effects of other light particles, such as hydrogen or lithium nuclei, in materials. Using μSR measurements of muons as proxy particles allow us to probe these effects in an extreme quantum limit, as the muon's low mass amplifies these quantum phenomena. This establishes μSR as a complementary tool for investigating the quantum behavior of light particles in crystal-lattice environments, where the muon itself acts as a quantum probe, thus providing a direct and quantitative benchmark of quantum-mechanical description of anharmonic effects.

In conclusion, we demonstrate that the quantum behavior of light particles—exemplified by the implanted muon in a μSR experiment—can significantly influence measurable properties in materials. This provides another experimental route to probe nuclear quantum phenomena with high spatial resolution and element specificity. This capability positions μSR as a powerful tool not only for interpreting muon behavior, but also for benchmarking quantum simulations of light particles in complex materials. Since nuclear quantum effects—including tunneling, zero-point motion, and anharmonicity—play a critical role in systems containing hydrogen and lithium, our approach opens a pathway to study and validate their behavior in materials such as hydrogen-bonded compounds and lithium-ion conductors. These insights are crucial for advancing fields ranging from energy storage and solid-state chemistry to quantum materials [1].

ACKNOWLEDGMENTS

F.H. acknowledges the financial support of the Swiss National Science Foundation through Program No. 192109. Experimental work was carried out at the Swiss Muon Source, PSI, Switzerland. The MERLIN HPC cluster, PSI, provided computing resources. Computing resources were also provided by the STFC Scientific Computing Department's SCARF cluster. M.G. and A.Z. acknowledge the financial support of the Slovenian Research and Innovation Agency through Program No. P1-0125 and Projects No. Z1-1852, No. N1-0148, No. J1-2461, No. J1-50008, No. J1-50012, No. N1-0356, No. N1-0345, and No. J2-60034.

DATA AVAILABILITY

The μSR data that support the findings in this Article are available at Ref. [37]. Other data are available from the authors upon reasonable request.

APPENDIX A: CLASSICAL MUON STOPPING SITES

Via a DFT + μ approach we have identified the classical muon stopping sites in Zn-barlowite [11,12] using the plane-wave DFT code CASTEP [38]. Using the MuFinder software [28], 32 initial muon candidates were put in low-symmetry positions, and after converging the geometry optimization below a 0.01 eV/Å force tolerance, the sites were clustered into four final candidate sites using connected-component clustering [28]. The calculations were performed in a supercell containing $2 \times 2 \times 1$ conventional unit cells of Zn-Barlowite [39] using the standard Perdew–Burke–Ernzerhof revised for solids (PBEsol) functional [40], an energy cutoff of 2000 eV, and a $2 \times 2 \times 3$ Monkhorst-Pack grid [41] for k-point sampling. The relatively high convergence parameters were used to ensure well-converged phonon calculations with the force converged to 10^{-4} eV/Å, well below the force tolerance of geometry optimization. The +1 charge state of the positive muon, which was modeled by an ultrasoft hydrogen pseudopotential with a reduced mass and an enhanced gyromagnetic ratio, was modeled by a +1 charge of the

TABLE II. The x, y, and z fractional coordinates of the muon stopping sites in the $2 \times 2 \times 1$ conventional unit cell for three different DFT functionals: LDA, PBE, and PBEsol. For all three functionals, a Hubbard $U_{\mathrm{eff}} = 5$ eV is used. The change in functionals leads to almost no change in the coordinates for the lowest-energy $(\mu\text{-OH})_1$ site, but a significant change in the y coordinate of the F-μ-Br site.

	LDA	PBE	PBEsol
F-μ-Br(x)	0.0747	0.0884	0.0733
F-μ-Br(y)	0.1533	0.1806	0.1506
F-μ-Br(z)	0.2488	0.2489	0.2489
$(\mu\text{-OH})_1(x)$	0.214	0.212	0.213
$(\mu\text{-OH})_1(y)$	0.109	0.1088	0.109
$(\mu\text{-OH})_1(z)$	0.221	0.222	0.222

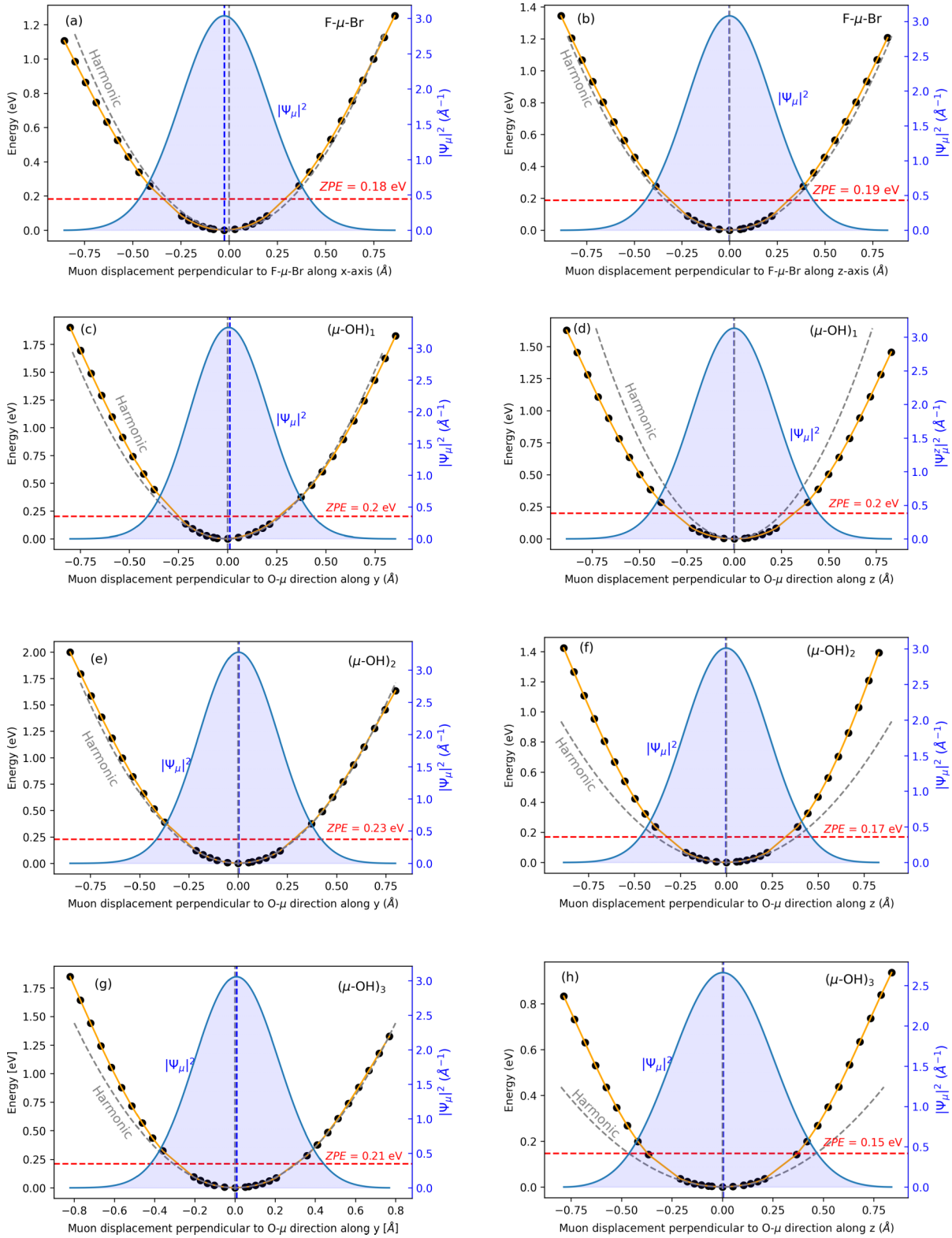

FIG. 4. Effective potentials in the weakly-bound adiabatic limit (relative to the classical energy) for muon displacements perpendicular to (a), (b) F-Br and (c)–(h) (μ-O)$_i$ directions at F-μ-Br and μ-OH sites, respectively, from DFT (black points, interpolated by orange curves). These are compared to the effective potential under the harmonic approximation (dashed gray). Also shown here, the quantum muon probability distributions $|\psi_\mu|^2$ in the adiabatic potentials (blue curves) with the resulting average muon displacements Δr_μ (dashed vertical blue lines) away from their classical/harmonic positions (dashed vertical gray lines).

supercell. All calculations were performed in a spin-polarized mode with an effective Hubbard $U_{\text{eff}} = U - J = 5$ eV, where U is the bare Hubbard interaction strength and J is Hund's coupling, consistently with previous studies [42–44]. To verify the reliability of our simulations, we have recalculated the coordinates of the converged F-μ-Br site and the lowest-energy (μ-OH)$_1$ site with different functionals and compared their values in Table II. We have compared the local density approximation (LDA) functional [45] and the Perdew-Burke-Ernzerhof (PBE) functional [46] to the PBEsol functional used in the rest of the paper.

APPENDIX B: ZERO-POINT ENERGY IN THE HARMONIC AND ADIABATIC APPROXIMATIONS

Γ-point phonon calculations were performed on a unit cell using CASTEP [38] with an energy cutoff of 2000 eV and a $4 \times 4 \times 3$ Monkhorst-Pack grid [41] using the standard PBEsol functional [40] and a finite-displacement method. This allowed us to estimate the muon's quantum zero-point energy (ZPE) in the harmonic approximation. Due to the low mass of the muon, the harmonic approximation underlying the phonon calculation is not *a priori* justified. Therefore, the effective adiabatic potential in the weakly bound limit [15] around the relaxed muon position was determined by sampling the muon energy at 35 different positions along the direction of the phonon normal modes of the muon. The adiabatic potential in the directions perpendicular to the main muon-ion direction (μ-O or F-μ-Br) are well described by the harmonic approximation and are summarized in Fig. 4, while those along it are strongly anharmonic (see Fig. 3 in the main text).

APPENDIX C: DETAILS ON THE μSR EXPERIMENTS

The zero-field (ZF) and longitudinal-field (LF) μSR experiments were performed on the FLexible Advanced MuSR Environment (FLAME) instrument at PSI located at the πM3.3 beamline of the HIPA complex at the Swiss Muon Source (SμS) at PSI. The sample was pressed into a pellet with a ≈6 mm diameter, glued with GE varnish to a ≈30-μm-thick copper foil and mounted on a sample holder fork close to a cold finger to ensure good thermal conductivity. The magnetic field at the sample position was measured with a Hall probe, while active zero-field compensation using vector magnets reduced the field under zero-field conditions to <1 μT. To be able to precisely measure the muon-nuclear spin oscillation, one has to collect much higher statistics than usual. For ZF measurement, 128 million muon/positron events were counted for the backward detector, and 127 million muons were in the forward detector. Between 25 million and 50 million events were gathered for the LF measurements. Data were fitted using the LMFIT Python package [47] using a microscopic approach outlined in Refs. [31,32,38]. The fitting parameters were obtained using Eq. (1). The muon stopping fractions were determined from a global fit performed simultaneously on all five spectra from different applied longitudinal fields B. While the dynamical relaxation rate λ_{dyn} was allowed to vary with applied field, it was constrained to be identical for all muon stopping sites at a given field. This

TABLE III. Fitting parameters in Eq. (1) in the main text, used to fit the measured spectra using three different descriptions of the muon: classical, shifted classical, and quantum (Fig. 2 in the main text). The fractions were determined from a global fit performed simultaneously over all spectra recorded at different applied longitudinal fields.

Classical						
B (mT)	f_s (%)	f_{FBr} (%)	f_{OH5} (%)	f_{OH4} (%)	λ_{dyn} (μs^{-1})	λ_{bgd} (μs^{-1})
0	84.9 ± 0.5	29.5 ± 1.1	0.5 ± 10	70 ± 3	0.13 ± 0.01	0.132 ± 0.009
0.5	same	same	same	same	0.12 ± 0.01	
1.0	same	same	same	same	0.039 ± 0.007	
2.06	same	same	same	same	0.018 ± 0.003	
4.25	same	same	same	same	0.012 ± 0.002	
Shifted Classical						
B (mT)	f_s (%)	f_{FBr} (%)	f_{OH5} (%)	f_{OH4} (%)	λ_{dyn} (μs^{-1})	λ_{bgd} (μs^{-1})
0	87.8 ± 0.4	40.7 ± 0.6	13.4 ± 2.1	45.9 ± 2.2	0.085 ± 0.006	0.127 ± 0.006
0.5	same	same	same	same	0.079 ± 0.005	
1.0	same	same	same	same	0.028 ± 0.003	
2.06	same	same	same	same	0.015 ± 0.002	
4.25	same	same	same	same	0.01 ± 0.001	
Quantum						
B (mT)	f_s (%)	f_{FBr} (%)	f_{OH5} (%)	f_{OH4} (%)	λ_{dyn} (μs^{-1})	λ_{bgd} (μs^{-1})
0	89.0 ± 0.3	46.7 ± 0.5	28.1 ± 1.9	25.2 ± 1.9	0.102 ± 0.004	0.093 ± 0.006
0.5	same	same	same	same	0.111 ± 0.003	
1.0	same	same	same	same	0.0326 ± 0.0023	
2.06	same	same	same	same	0.0175 ± 0.0010	
4.25	same	same	same	same	0.0113 ± 0.0007	

restriction reduces the number of free parameters and prevents overfitting. For the same reason, the background relaxation rate was kept constant across all applied fields. All free fitting parameters are reported in Table III. We see that the dynamical relaxation rate decreases with increasing field, consistent with the progressive decoupling of the dynamically fluctuating Cu^{2+} magnetic moments. Importantly, the muon stopping site positions were never treated as adjustable parameters but were taken from the *ab initio* calculations and the quantum muon wave function, as the static polarization functions $P_i^{\mathrm{stat}}(t)$ were calculated directly from the known crystallographic structure. To properly treat the muon as a quantum-mechanical particle, its dipolar Hamiltonian was averaged over the three-dimensional probability distribution of the muon $|\psi_\mu|^2$, as in Refs. [15,16]. For each muon, the three-dimensional probability distribution consists of the three one-dimensional adiabatic potentials along the principal phonon modes of the muon (see previous section), and was numerically sampled using a $30 \times 30 \times 30$ rectangular mesh. Due to computational limitations, the Hamiltonian was truncated to a dimension of 256, taking into account only interactions with the seven nuclei with spin $I > 0$ closest to the muon at a given muon site.

[1] T. E. Markland and M. Ceriotti, Nuclear quantum effects enter the mainstream, Nat. Rev. Chem. **2**, 0109 (2018).

[2] U. Ranieri, L. J. Conway, M.-E. Donnelly, H. Hu, M. Wang, P. Dalladay-Simpson, M. Peña-Alvarez, E. Gregoryanz, A. Hermann, and R. T. Howie, Formation and stability of dense methane-hydrogen compounds, Phys. Rev. Lett. **128**, 215702 (2022).

[3] G. J. Ackland, M. Dunuwille, M. Martinez-Canales, I. Loa, R. Zhang, S. Sinogeikin, W. Cai, and S. Deemyad, Quantum and isotope effects in lithium metal, Science **356**, 1254 (2017).

[4] A. Drozdov, M. Eremets, I. Troyan, V. Ksenofontov, and S. I. Shylin, Conventional superconductivity at 203 kelvin at high pressures in the sulfur hydride system, Nature (London) **525**, 73 (2015).

[5] M. I. Eremets, V. S. Minkov, A. P. Drozdov, P. Kong, V. Ksenofontov, S. I. Shylin, S. L. Bud'ko, R. Prozorov, F. F. Balakirev, D. Sun, *et al.*, High-temperature superconductivity in hydrides: Experimental evidence and details, J. Supercond. Novel Magn. **35**, 965 (2022).

[6] M. Rossi, P. Gasparotto, and M. Ceriotti, Anharmonic and quantum fluctuations in molecular crystals: A first-principles study of the stability of paracetamol, Phys. Rev. Lett. **117**, 115702 (2016).

[7] Y. Litman, V. Kapil, Y. M. Y. Feldman, D. Tisi, T. Begušić, K. Fidanyan, G. Fraux, J. Higer, M. Kellner, T. E. Li, E. S. Pós, E. Stocco, G. Trenins, B. Hirshberg, M. Rossi, and M. Ceriotti, i-pi 3.0: A flexible and efficient framework for advanced atomistic simulations, J. Chem. Phys. **161**, 062504 (2024).

[8] S. J. Blundell, R. De Renzi, T. Lancaster, and F. L. Pratt, *Muon Spectroscopy: An Introduction* (Oxford University Press, Oxford, UK, 2021).

[9] A. Yaouanc and P. D. De Reotier, *Muon Spin Rotation, Relaxation, and Resonance: Applications to Condensed Matter*, International Series of Monographs on Physics No. 147 (Oxford University Press, Oxford, UK, 2011).

[10] A. Amato and E. Morenzoni, *Introduction to Muon Spin Spectroscopy: Applications to Solid State and Material Sciences* (Springer, Berlin, 2024).

[11] J. S. Möller, D. Ceresoli, T. Lancaster, N. Marzari, and S. J. Blundell, Quantum states of muons in fluorides, Phys. Rev. B **87**, 121108(R) (2013).

[12] S. Blundell and T. Lancaster, DFT + μ: Density functional theory for muon site determination, Appl. Phys. Rev. **10**, 021316 (2023).

[13] A. Amato, P. Dalmas de Réotier, D. Andreica, A. Yaouanc, A. Suter, G. Lapertot, I. M. Pop, E. Morenzoni, P. Bonfà, F. Bernardini, and R. De Renzi, Understanding the μSR spectra of MnSi without magnetic polarons, Phys. Rev. B **89**, 184425 (2014).

[14] F. R. Foronda, F. Lang, J. S. Möller, T. Lancaster, A. T. Boothroyd, F. L. Pratt, S. R. Giblin, D. Prabhakaran, and S. J. Blundell, Anisotropic local modification of crystal field levels in Pr-based pyrochlores: A muon-induced effect modeled using density functional theory, Phys. Rev. Lett. **114**, 017602 (2015).

[15] M. Gomilšek, F. L. Pratt, S. P. Cottrell, S. J. Clark, and T. Lancaster, Many-body quantum muon effects and quadrupolar coupling in solids, Commun. Phys. **6**, 142 (2023).

[16] I. J. Onuorah, P. Bonfà, R. De Renzi, L. Monacelli, F. Mauri, M. Calandra, and I. Errea, Quantum effects in muon spin spectroscopy within the stochastic self-consistent harmonic approximation, Phys. Rev. Mater. **3**, 073804(R) (2019).

[17] S. Mañas-Valero, B. M. Huddart, T. Lancaster, E. Coronado, and F. L. Pratt, Quantum phases and spin liquid properties of 1T-TaS_2, npj Quantum Mater. **6**, 69 (2021).

[18] W. Yuan, J. Wang, P. M. Singer, R. W. Smaha, J. Wen, Y. S. Lee, and T. Imai, Emergence of the spin polarized domains in the kagome lattice Heisenberg antiferromagnet Zn-barlowite $(Zn_{0.95}Cu_{0.05})Cu_3(OD)_6FBr$, npj Quantum Mater. **7**, 120 (2022).

[19] J. Wang, W. Yuan, P. M. Singer, R. W. Smaha, W. He, J. Wen, Y. S. Lee, and T. Imai, Freezing of the lattice in the kagome lattice Heisenberg antiferromagnet Zn-barlowite $ZnCu_3(OD)_6FBr$, Phys. Rev. Lett. **128**, 157202 (2022).

[20] Z. Feng, Z. Li, X. Meng, W. Yi, Y. Wei, J. Zhang, Y.-C. Wang, W. Jiang, Z. Liu, S. Li, *et al.*, Gapped spin-1/2 spinon excitations in a new kagome quantum spin liquid compound $Cu_3Zn(OH)_6FBr$, Chin. Phys. Lett. **34**, 077502 (2017).

[21] K. Tustain, B. Ward-O'Brien, F. Bert, T. Han, H. Luetkens, T. Lancaster, B. M. Huddart, P. J. Baker, and L. Clark, From magnetic order to quantum disorder in the Zn-barlowite series of $S = 1/2$ kagomé antiferromagnets, npj Quantum Mater. **5**, 74 (2020).

[22] L. Savary and L. Balents, Quantum spin liquids: A review, Rep. Prog. Phys. **80**, 016502 (2017).

[23] P. Mendels and F. Bert, Quantum kagome frustrated antiferromagnets: One route to quantum spin liquids, C. R. Phys. **17**, 455 (2016).

[24] C. Broholm, R. J. Cava, S. A. Kivelson, D. G. Nocera, M. R. Norman, and T. Senthil, Quantum spin liquids, Science **367**, eaay0668 (2020).

[25] J. Wang, W. Yuan, P. M. Singer, A. Schneidewind, D. T. Adroja, A. Zorko, J. G. Cheng, and M. Fu, Emergence of spin singlets

with inhomogeneous gaps in the kagome lattice Heisenberg antiferromagnets Zn-barlowite and herbertsmithite, Nat. Phys. **17**, 1109 (2021).

[26] S. Yan, D. A. Huse, and S. R. White, Spin-liquid ground state of the $S = 1/2$ kagome Heisenberg antiferromagnet, Science **332**, 1173 (2011).

[27] J. Khatua, B. Sana, A. Zorko, M. Gomilšek, K. Sethupathi, M. R. Rao, M. Baenitz, B. Schmidt, and P. Khuntia, Experimental signatures of quantum and topological states in frustrated magnetism, Phys. Rep. **1041**, 1 (2023).

[28] B. Huddart, A. Hernández-Melián, T. Hicken, M. Gomilšek, Z. Hawkhead, S. Clark, F. Pratt, and T. Lancaster, Mufinder: A program to determine and analyse muon stopping sites, Comput. Phys. Commun. **280**, 108488 (2022).

[29] S. Baroni, S. de Gironcoli, A. Dal Corso, and P. Giannozzi, Phonons and related crystal properties from density-functional perturbation theory, Rev. Mod. Phys. **73**, 515 (2001).

[30] J. S. Lord, Computer simulation of muon spin evolution, Physica B **374-375**, 472 (2006).

[31] J. S. Lord, S. Cottrell, and W. Williams, Muon spin relaxation in strongly coupled systems, Physica B **289-290**, 495 (2000).

[32] J. M. Wilkinson and S. J. Blundell, Information and decoherence in a muon-fluorine coupled system, Phys. Rev. Lett. **125**, 087201 (2020).

[33] M. Celio, New method to calculate the muon polarization function, Phys. Rev. Lett. **56**, 2720 (1986).

[34] P. Bonfà, J. Frassineti, J. M. Wilkinson, G. Prando, M. M. Isah, C. Wang, T. Spina, B. Joseph, V. F. Mitrović, R. De Renzi, S. J. Blundell, and S. Sanna, Entanglement between muon and $I > \frac{1}{2}$ nuclear spins as a probe of charge environment, Phys. Rev. Lett. **129**, 097205 (2022).

[35] R. Wang, X. Li, X. Han, J. Lin, Y. Wang, T. Qian, H. Ding, Y. Shi, and X. Liu, X-ray absorption investigation of the site occupancies of the copper element in nominal $ZnCu_3(OH)_6FBr$, Chin. Phys. B **30**, 046102 (2021).

[36] R. S. Hayano, Y. J. Uemura, J. Imazato, N. Nishida, T. Yamazaki, and R. Kubo, Zero-and low-field spin relaxation studied by positive muons, Phys. Rev. B **20**, 850 (1979).

[37] https://musruser.psi.ch/cgi-bin/SearchDB.cgi

[38] S. J. Clark, M. D. Segall, C. J. Pickard, P. J. Hasnip, M. I. J. Probert, K. Refson, and M. C. Payne, First principles methods using CASTEP, Z. Kristallogr. - Cryst. Mater. **220**, 567 (2005).

[39] T. Björkman, CIF2Cell: Generating geometries for electronic structure programs, Comput. Phys. Commun. **182**, 1183 (2011).

[40] J. P. Perdew, A. Ruzsinszky, G. I. Csonka, O. A. Vydrov, G. E. Scuseria, L. A. Constantin, X. Zhou, and K. Burke, Restoring the density-gradient expansion for exchange in solids and surfaces, Phys. Rev. Lett. **100**, 136406 (2008).

[41] H. J. Monkhorst and J. D. Pack, Special points for Brillouin-zone integrations, Phys. Rev. B **13**, 5188 (1976).

[42] V. I. Anisimov, J. Zaanen, and O. K. Andersen, Band theory and Mott insulators: Hubbard U instead of stoner I, Phys. Rev. B **44**, 943 (1991).

[43] D. Guterding, R. Valentí, and H. O. Jeschke, Reduction of magnetic interlayer coupling in barlowite through isoelectronic substitution, Phys. Rev. B **94**, 125136 (2016).

[44] H. O. Jeschke, F. Salvat-Pujol, E. Gati, N. H. Hoang, B. Wolf, M. Lang, J. A. Schlueter, and R. Valentí, Barlowite as a canted antiferromagnet: Theory and experiment, Phys. Rev. B **92**, 094417 (2015).

[45] W. Kohn and L. J. Sham, Self-consistent equations including exchange and correlation effects, Phys. Rev. **140**, A1133 (1965).

[46] J. P. Perdew, K. Burke, and Y. Wang, Generalized gradient approximation for the exchange-correlation hole of a many-electron system, Phys. Rev. B **54**, 16533 (1996).

[47] M. Newville, T. Stensitzki, D. B. Allen, M. Rawlik, A. Ingargiola, and A. Nelson, LMFIT: Non-linear least-square minimization and curve-fitting for Python, Astrophys. Source Code Lib. ascl (2016).